

Quantum Metric Enhancement and Hierarchical Scaling in One-Dimensional Quasiperiodic Systems

Jundi Wang,^{1,*} Yuxiao Chen,^{1,*} and Huaqing Huang^{1,2,3,†}

¹*School of Physics, Peking University, Beijing 100871, China*

²*Collaborative Innovation Center of Quantum Matter, Beijing 100871, China*

³*Center for High Energy Physics, Peking University, Beijing 100871, China*

(Dated: July 8, 2025)

The quantum metric, a key component of quantum geometry, plays a central role in a wide range of physical phenomena and has been extensively studied in periodic crystals and moiré materials. Here, we systematically investigate quantum geometry in one-dimensional (1D) quasiperiodic systems and uncover novel properties that fundamentally distinguish them from both periodic crystals and disordered media. Our comparative analysis reveals that quasiperiodicity significantly enhances the quantum metric—despite the absence of translational symmetry—due to the presence of critical wavefunctions with long-range spatial correlations. In the Aubry-André-Harper model, we show that the quantum metric serves as a sensitive probe of localization transitions, exhibiting sharp changes at the critical point and distinct behaviors near mobility edges. In the Fibonacci chain, characterized by a singular continuous spectrum, we discover an anomalous enhancement of the quantum metric when the Fermi level lies within the minimal gaps of the fractal energy spectrum. Using a perturbative renormalization group framework, we trace this enhancement to the hierarchical structure of the spectrum and the bonding-antibonding nature of critical states across narrow gaps. Our findings establish a fundamental connection between wavefunction criticality, spectral fractality, and quantum geometry, suggesting quasiperiodic systems as promising platforms for engineering enhanced quantum geometric properties beyond conventional crystalline paradigms.

I. INTRODUCTION

The quantum metric tensor is a central geometric quantity in quantum mechanics that characterizes the local distance between neighboring quantum states in Hilbert space [1, 2]. It arises as the real part of the quantum geometric tensor, whose imaginary part corresponds to the Berry curvature. While the Berry curvature governs topological phenomena such as the anomalous Hall effect [3], the quantum metric captures geometric aspects of quantum states and has recently been recognized for its pivotal role in a broad range of material properties [4–8]. For example, it underlies intrinsic nonlinear conductivities in noncentrosymmetric systems, enabling novel optoelectronic responses even in topologically trivial materials [9–17]. Moreover, recent works show that quantum metric contributes significantly to correlation effects, including fractional Chern insulators [18–20], exciton condensations [21, 22], and flat-band superconductivity in moiré systems [23–26]. Despite growing interest in the quantum metric in periodic and disordered systems, its behavior in quasiperiodic systems remains largely unexplored. This omission is notable given that quasiperiodic systems occupy a unique intermediate regime between order and disorder, with long-range order but no translational symmetry. Their singular continuous spectra and unconventional localization transitions suggest the potential for distinct quantum geometric phenomena.

One-dimensional quasiperiodic systems provide a versatile platform for investigating such effects. These systems, exemplified by the Fibonacci chain (FC) and the Aubry-André-Harper (AAH) model, display exotic electronic and topological properties arising from deterministic aperiodicity [27–34]. The FC is constructed via substitution rules to mimic quasicrystalline order [27], exhibits a singular continuous spectrum and multifractal eigenstates, while the AAH model with a cosine-modulated potential [33, 34] hosts a tunable localization transition driven by potential strength. In its generalized form, the AAH model can also exhibit mobility edges in 1D, featuring energy-dependent localization transitions that are prohibited in conventional randomly disordered 1D systems [35, 36]. Furthermore, deep connections emerge from topological equivalence: the FC can be mapped to a critical point of the AAH model under specific parameterizations, sharing topological invariants and boundary modes that are associated with the “ancestor” 2D lattice model describing the integer quantum Hall effect [31]. Experimental realizations in photonic lattices [30], cold atom systems [37], and acoustic metamaterials [38] have made these quasiperiodic systems accessible platforms for probing quantum localization, transport, and topology.

In this work, we systematically investigate the quantum metric in 1D quasiperiodic systems and uncover its unique features and physical origins. First, we compute the quantum metric in representative quasiperiodic models and find its magnitude significantly enhanced compared to disordered systems. We attribute this enhancement to the critical nature of quasiperiodic wavefunctions, which exhibit long-range spatial correlations despite the lack of translational symmetry. Focusing on

* These authors contributed equally to this work.

† Contact author: huaqing.huang@pku.edu.cn

the AAH model, we analyze the evolution of the quantum metric across localization-delocalization transitions. By tuning the Fermi level across mobility edges, we show that the quantum metric sharply reflects the localization properties of the occupied states. We then turn to the FC, a paradigmatic quasicrystal with a self-similar, fractal energy spectrum. We find that the quantum metric displays pronounced peaks when the Fermi level resides within the narrow gaps of the fractal spectrum. To explain this, we employ a perturbative renormalization group analysis, showing that these peaks originate from the hierarchical gap structure and the bonding-antibonding nature of critical wavefunctions across small gaps. Our findings establish a fundamental link between spectral fractality and quantum geometry, positioning quasiperiodic systems as promising platforms for realizing enhanced geometric responses and advancing quantum geometric engineering beyond the limits of periodic systems.

II. MODEL AND METHODS

A. One-Dimensional Quasiperiodic Models

One-dimensional quasiperiodic systems occupy a unique position between perfectly ordered crystals and completely disordered systems. Characterized by long-range order without translational symmetry, they host rich spectral and transport phenomena. In this section, we focus on two paradigmatic models, the FC and the AAH model, as representative systems for investigating the quantum geometric properties of quasiperiodic wavefunctions.

1. Fibonacci Chain

The FC is a prototypical 1D quasiperiodic system constructed through deterministic substitution rules that encode long-range aperiodic order. Unlike random disorder, quasiperiodicity in the Fibonacci sequence leads to well-defined structural correlations and generates characteristic spectral and localization features.

The Fibonacci sequence $\{F_n\}$ is constructed by the substitution rules $A \rightarrow AB$, $B \rightarrow A$, beginning from an initial seed. This recursive procedure generates sequences such as A , AB , ABA , $ABAAB$, and so on. The lengths of the letters in the n -th sequence are equal to the Fibonacci numbers F_n , which are defined by the recursion relation $F_n = F_{n-1} + F_{n-2}$ with $F_0 = F_1 = 1$. In the thermodynamic limit, the ratio of the number of A and B units approaches the golden mean $\tau = (1 + \sqrt{5})/2$, reflecting the incommensurability intrinsic to the structure. The lengths of the chains are given by $F_n \sim \tau^n$ in the large n limit.

The tight-binding Hamiltonian for the FC takes the

general form [27, 28]:

$$H = \sum_n \epsilon_n c_n^\dagger c_n - (t_n c_{n+1}^\dagger c_n + \text{h.c.}), \quad (1)$$

where c_n^\dagger (c_n) creates (annihilates) an electron at site n , ϵ_n represents the on-site energy, and t_n denotes the hopping amplitude between adjacent sites n and $n + 1$.

Two distinct variants of the Fibonacci model are commonly studied:

1. *Off-diagonal FC*: The hopping amplitudes t_n follow the Fibonacci sequence, taking values t_A or t_B according to the sequence elements A or B, while site energies remain uniform ($\epsilon_n = \epsilon_0$). This model exhibits particular mathematical elegance due to its self-similar renormalization properties.
2. *Diagonal FC*: The on-site energies ϵ_n take values ϵ_A or ϵ_B following the Fibonacci sequence, while hopping amplitudes remain constant ($t_n = t$). This variant has been extensively studied in optical experiments and shares many spectral features with its off-diagonal counterpart.

A key feature of the FC is its singular continuous energy spectrum, which lies between the absolutely continuous spectrum of periodic systems and the pure point spectrum of disordered systems. The spectrum exhibits a self-similar, Cantor-set structure with hierarchically nested energy gaps, reflecting the underlying renormalization symmetry of the lattice [39, 40]. Correspondingly, eigenstates are neither extended nor exponentially localized but are instead critical: they decay algebraically and display multifractal scaling [41].

Remarkably, the FC exhibits critical wavefunctions for any finite quasiperiodic modulation strength. This critical behavior makes the FC an ideal platform for probing quantum geometric signatures associated with criticality and multifractality.

2. Aubry-André-Harper Model

The AAH model introduces quasiperiodicity through an incommensurate cosine potential, rather than a substitution sequence. Its Hamiltonian is given by [33, 34]:

$$H = \sum_n (t c_{n+1}^\dagger c_n + \text{h.c.}) + V \cos(2\pi\omega n + \phi) c_n^\dagger c_n, \quad (2)$$

where t represents the nearest-neighbor hopping amplitude, V controls the potential strength, ϕ is an arbitrary phase factor which is also known as the phason parameter [42, 43], and ω is an irrational number (typically the golden ratio $(\sqrt{5} - 1)/2$) ensuring the potential's incommensurability with the underlying lattice [33, 34]. This model has deep connections to the physics of electrons in a magnetic field. When derived as a dimensional reduction of a two-dimensional (2D) Hofstadter problem, ω

plays the role of the magnetic flux per plaquette, connecting the model to the fractal Hofstadter butterfly spectrum [44].

Unlike the FC where all states are critical, the AAH model exhibits a sharp metal-insulator transition at the critical value $V_c = 2t$. For $V < 2t$, all eigenstates are extended with properties similar to Bloch waves, while for $V > 2t$, all states become exponentially localized [33]. At the critical point $V_c = 2t$, the model is self-dual under a generalized Fourier transform that maps between position and momentum representations. This duality manifests in critical states with multifractal properties similar to those observed in the FC.

The AAH model can be generalized to incorporate mobility edges—energy boundaries separating localized states from extended or critical states within the same spectrum—a feature typically forbidden in conventional one-dimensional disordered systems according to scaling theory. One such generalization modifies the on-site potential to create energy-dependent localization behavior [35]:

$$V_n = v \frac{1 - \cos(2\pi n\alpha + \delta)}{1 + \beta \cos(2\pi n\alpha + \delta)}, \quad (3)$$

where v determines the overall potential strength, α is an irrational number (typically $(\sqrt{5} - 1)/2$), δ represents a phase factor, and β is the critical deformation parameter that generates the mobility edge. At $\beta = 0$, the model reduces to the original AAH model, while for finite β , the energy spectrum supports a mobility edge at $E = 2\text{sgn}(v)(1 - |v|)/\beta$, creating a well-defined boundary between extended and localized states.

Another model that implements analytically tractable mobility edges arranges both hopping and on-site terms in a mosaic pattern [45]:

$$\{t_n, V_n\} = \begin{cases} \{\lambda, 2t_0 \cos[2\pi\alpha(n-1) + \delta]\}, & n = 1 \bmod \kappa, \\ 2t_0 \cos(2\pi\alpha n + \delta)\{1, 1\}, & n = 0 \bmod \kappa, \\ \{\lambda, 0\}, & \text{otherwise.} \end{cases} \quad (4)$$

where κ is an integer and $\kappa \geq 2$, λ and δ are hopping coefficient and phase offset, respectively. This construction creates sharp mobility edges at $E = \pm\lambda$ with critical states between these boundaries and localized states outside them. It offers a tunable framework for studying energy-resolved transitions in quantum geometry.

B. Quantum Metric

1. Formulation of quantum metric

The quantum metric tensor is a fundamental quantity in quantum geometry, capturing the infinitesimal distance between neighboring quantum states in Hilbert space. In translationally invariant crystalline systems, it is defined via derivatives of the Bloch wavefunctions

with respect to crystal momentum. For a set of occupied Bloch bands, the quantum geometric tensor is given by [46]:

$$Q_{\mu\nu}^{ab}(\mathbf{k}) = \langle \partial_\mu u_{\mathbf{k}}^a | [\mathbb{I} - P_{\mathbf{k}}] | \partial_\nu u_{\mathbf{k}}^b \rangle, \quad (5)$$

where $u_{\mathbf{k}}^a$ is the periodic part of the Bloch wavefunction for band a , $\partial_\mu = \partial/\partial k_\mu$ denotes momentum derivatives with $\mu, \nu \in \{x, y, z\}$, and $P_{\mathbf{k}} = \sum_{a \in \text{occ}} |u_{\mathbf{k}}^a\rangle\langle u_{\mathbf{k}}^a|$ is the projector onto occupied bands. The tensor $Q_{\mu\nu}^{ab}(\mathbf{k})$ naturally decomposes into real and imaginary parts:

$$Q_{\mu\nu}^{ab}(\mathbf{k}) = g_{\mu\nu}^{ab}(\mathbf{k}) + \frac{i}{2} \Omega_{\mu\nu}^{ab}(\mathbf{k}), \quad (6)$$

where $g_{\mu\nu}^{ab}(\mathbf{k})$ is the quantum metric (real and symmetric), and $\Omega_{\mu\nu}^{ab}(\mathbf{k})$ is the Berry curvature (imaginary and antisymmetric). When integrating the quantum geometric tensor over the Brillouin zone and tracing over all occupied bands, we arrive at

$$\begin{aligned} \mathcal{Q}_{\mu\nu} &= \int_{\text{BZ}} d\mathbf{k} \text{Tr}[Q_{\mu\nu}^{ab}(\mathbf{k})] \\ &= \int_{\text{BZ}} d\mathbf{k} \sum_{a \in \text{occ}} \langle \partial_\mu u_{\mathbf{k}}^a | (\mathbb{I} - |u_{\mathbf{k}}^a\rangle\langle u_{\mathbf{k}}^a|) | \partial_\nu u_{\mathbf{k}}^a \rangle. \end{aligned} \quad (7)$$

The real part, $\mathcal{G}_{\mu\nu} = \text{Re}[\mathcal{Q}_{\mu\nu}]$, defines the integrated quantum metric. Importantly, the trace of $\mathcal{G}_{\mu\nu}$ corresponds to the gauge-invariant part of the localization functional for maximally localized Wannier functions [46, 47], highlighting the deep connection between quantum geometry and electronic localization.

However, this momentum-space formalism presumes the existence of translational symmetry and well-defined Bloch states, rendering it inapplicable to systems such as disordered or quasiperiodic lattices. To overcome this limitation, we adopt a real-space representation of the quantum geometric tensor, defined through the projected position operator [46, 48]:

$$\mathcal{Q}_{\mu\nu} = \text{Tr}[P \hat{r}_\mu (1 - P) \hat{r}_\nu P], \quad (8)$$

where $P = \sum_{\alpha \in \text{occ}} |\psi_\alpha\rangle\langle\psi_\alpha|$ is the projector onto the occupied subspace, and \hat{r}_μ is the position operator along the μ -direction, serving as a real-space analog of momentum derivatives.

In 1D systems, the position operator reduces to $\hat{\mathbf{r}} = \hat{x}$, and \mathcal{Q}_{xx} becomes real-valued, thus equaling the integrated quantum metric:

$$\mathcal{G}_{xx} = \text{Re}[\mathcal{Q}_{xx}] = \mathcal{Q}_{xx}. \quad (9)$$

Physically, this real-space formulation quantifies the spread of occupied-state wavefunctions, with connections to the modern theory of polarization and localization [2, 6]. In particular, the quantum metric can be understood as a measure of the mean-square quantum fluctuation of position within the occupied subspace [46]:

$$\mathcal{G}_{xx} \sim \langle x^2 \rangle - \langle x \rangle^2, \quad (10)$$

where the average is taken over the occupied states. Systems with more spatially extended occupied states correspondingly exhibit larger \mathcal{G}_{xx} .

Beyond wavefunction spread, the quantum metric also encodes the degree of spatial correlation among occupied states [49]. From this perspective, large quantum metric values indicate stronger non-local correlations and greater wavefunction overlap between different states, while small values suggest more localized, weakly correlated states. This interpretation proves particularly valuable for understanding systems with critical or multifractal wavefunctions, where long-range quantum coherence persists despite the lack of periodic order.

2. Numerical Implementation

In our numerical calculations, we evaluate the quantum metric by directly computing matrix elements between eigenstates. For each system size N , we first diagonalize the Hamiltonian to obtain the complete set of eigenstates $\{|\psi_\alpha\rangle\}$ and corresponding energies $\{E_\alpha\}$. The projector onto occupied states below the Fermi energy E_F is constructed as $P = \sum_{E_\alpha \leq E_F} |\psi_\alpha\rangle\langle\psi_\alpha|$. The position operator \hat{x} is represented as a diagonal matrix in the site basis: $\hat{x} = \sum_{i=1}^N x_i |i\rangle\langle i|$, where x_i denotes the coordinate of site i .

To examine the Fermi-energy dependence of the quantum metric, we utilize an equivalent expression based on the sum over interband matrix elements:

$$\mathcal{G}(E_F) = \sum_{\alpha \in \text{occ}, \beta \in \text{unocc}} |\langle\psi_\alpha|\hat{x}|\psi_\beta\rangle|^2 \quad (11)$$

$$= \sum_{E_\alpha < E_F < E_\beta} |\langle\psi_\alpha|\hat{x}|\psi_\beta\rangle|^2. \quad (12)$$

We omit the subscript for brevity where unambiguous. This pairwise decomposition reveals how individual transitions across the Fermi surface contribute to the overall quantum metric. Transitions between spatially overlapping but orthogonal states near E_F typically yield the dominant contributions.

To disentangle the effects of quasiperiodicity from those of statistical disorder, we generate control systems by randomly reshuffling either the on-site energies or hopping amplitudes (depending on where the quasiperiodicity is introduced in the quasicrystal models) while maintaining their respective distributions. All numerical calculations are performed with open boundary conditions to eliminate spurious effects arising from artificial periodicity.

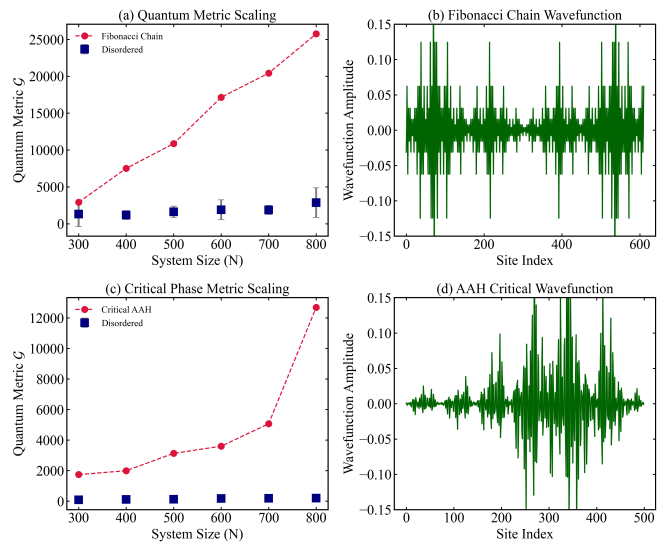


FIG. 1. Quantum metric enhancement in quasiperiodic systems. (a) and (c) Scaling relationship between quantum metric \mathcal{G} at half filling and system size N for the FC (off-diagonal, $t_A = 1$, $t_B = 2$) and critical AAH models ($V = 2t$, $\omega = (\sqrt{5} - 1)/2$) (crimson circles) compared with their disorder-averaged counterparts (navy squares with error bars). (b) and (d) Representative critical wavefunctions of the states at half filling for the FC and critical AAH models.

III. NUMERICAL RESULTS

A. Enhanced Quantum Metric in Quasiperiodic Systems

To systematically investigate the geometric properties inherent to quasiperiodicity, we calculate the integrated quantum metric \mathcal{G} at half-filling for both the off-diagonal FC and the AAH model at its critical point. For direct comparison, we also construct disordered reference systems by randomly permuting quasiperiodic modulations in each model, thereby preserving the statistical distribution of parameters while eliminating long-range order. This controlled framework isolates the intrinsic contribution from quasiperiodicity itself, as opposed to those arising generally from broken translational symmetry.

Despite the fact that both quasiperiodic and disordered systems lack translational symmetry, the quasiperiodic systems exhibit significantly enhanced quantum metric compared to the corresponding disordered systems. As shown in Fig. 1(a), the FC (crimson circles) exhibits larger values of \mathcal{G} than its disordered counterpart (navy squares) across all system sizes examined ($N = 300-800$). A similar enhancement is also observed in Fig. 1(c) for the critical AAH model at $V = 2t$: the quasiperiodic system again outperforms its randomized analog. Notably, while the disordered systems exhibit nearly size-independent metric values, the quasiperiodic systems show robust scaling of the quantum metric with system size. This scaling behavior demonstrates that the en-

enhancement persists across length scales and reflects the intrinsic geometric structure encoded in the quasiperiodic order. These results indicate that it is the quasiperiodicity, which is characterized by a deterministic but non-periodic arrangement, rather than just the absence of translation symmetry, that plays an active role in enhancing quantum geometric properties.

The origin of this enhancement can be traced to the spatial characteristics of the eigenstate wavefunctions in quasiperiodic systems. As described in Eq.(10), the quantum metric effectively measures the second moment of position over the occupied states, thereby capturing both wavefunction delocalization and spatial correlations. Fig. 1(b) and 1(d) display representative wavefunctions for the FC and the critical AAH models. In both cases, the critical wavefunctions display multifractal characteristics: amplitude distributions exhibit power-law decay with pronounced fluctuations across multiple length scales, reflecting the self-similar nature of the underlying quasiperiodic modulation. In the FC [Fig.1(b)], the hierarchical spatial structure directly mirrors the substitutional rule defining the lattice, while in the AAH model [Fig.1(d)], the fractal scaling and self-similarity reflect the model's self-duality at the critical point $V = 2t$. Despite their distinct microscopic origins, both systems support critical states that are neither fully extended nor exponentially localized. Crucially, these critical states retain long-range coherence and sufficient spatial correlations, which are key ingredients for sustaining large quantum metric values.

In contrast, the disordered systems host exponentially localized wavefunctions that decay rapidly from their localization centers, effectively eliminating long-range spatial correlations [50, 51]. This localization suppresses the quantum metric, resulting in significantly smaller values. Thus, the enhanced quantum metric observed in quasiperiodic systems arises from the presence of critical wavefunctions that combine spatial nonlocality with fractal structure, offering a fundamental mechanism distinct from that of either ordered or disordered systems.

B. Quantum Metric Across Localization Transitions

The AAH model provides an ideal platform for investigating how quantum geometric properties evolve across localization transitions, offering a tunable quasiperiodic potential strength V that can drive the system between extended, critical, and localized phases. We performed a comprehensive analysis of the integrated quantum metric \mathcal{G} in an AAH model of size $L = 500$ by varying the parameter V . Fig. 2 presents the quantum metric at half-filling as a function of V , revealing a striking correlation between quantum geometry and the localization properties of the system. In the extended phase ($V < 2t$), the quantum metric maintains consistently high values, reflecting the extensive spatial overlap between delocalized

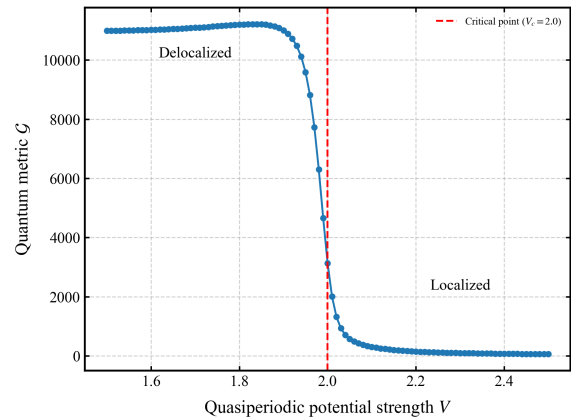


FIG. 2. Quantum metric \mathcal{G} as an indicator of localization transitions in the AAH model [Eq. (2)]. The blue curve shows the quantum metric \mathcal{G} at half-filling of a 500-site system, plotted as a function of quasiperiodic potential strength V (normalized by hopping amplitude t). The vertical red dashed line marks the critical point $V_c = 2t$.

eigenstates. As V approaches the critical point $V_c = 2t$, \mathcal{G} undergoes a sharp decline, with the steepest drop occurring precisely at the transition. This sharp change directly mirrors the evolution of the eigenstate character: wavefunctions in the extended phase are delocalized over the entire system, supporting strong quantum geometric responses, whereas in the localized phase ($V > 2t$), wavefunctions are exponentially confined, leading to a suppression of spatial correlations and thus a diminished quantum metric.

This behavior highlights the quantum metric as a sensitive and nonlocal probe of localization transitions, capable of detecting abrupt changes in wavefunction character that are often invisible to conventional local observables. Notably, the sharpness of the drop in \mathcal{G} near the critical point underscores a unique feature of localization transitions induced by quasiperiodicity. These results establish the quantum metric as a powerful diagnostic for characterizing localization phenomena in quasiperiodic systems.

Beyond the standard AAH model, we extend our analysis to the generalized AAH model [Eq. (3)] and the mosaic model [Eq. (4)], both of which exhibit mobility edges that separate localized states from extended or critical states within the same spectrum. To characterize the localization properties of individual eigenstates, we calculate their fractal dimension (FD)[52]:

$$\text{FD} = - \lim_{N \rightarrow \infty} \frac{\ln(\sum_j |u_{m,j}|^4)}{\ln N}, \quad (13)$$

where $u_{m,j}$ is the amplitude of the m -th eigenstate at site j , and N is the system size. This quantity approaches 1 for fully extended states, 0 for localized states, and assumes intermediate values for critical states.

Fig. 3 presents a detailed analysis of mobility edges and their quantum geometric signatures. Panels (a) and

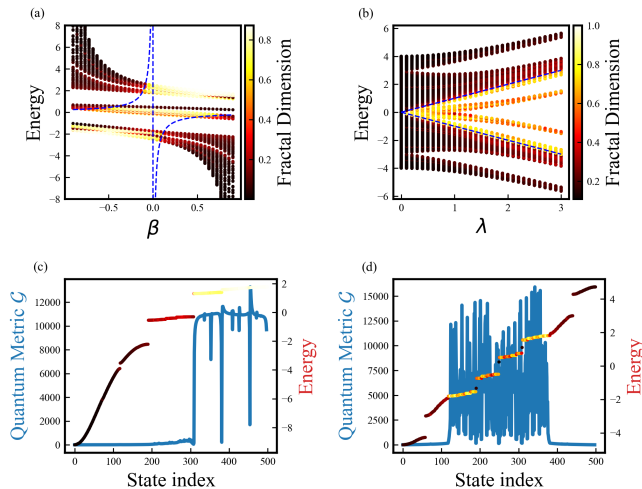


FIG. 3. (a) Energy spectrum vs. deformation parameter β for the generalized AAH model in Eq. (3), calculated for a lattice of $L = 300$ sites with parameters $t = 1$, $v = -1.8$, $\alpha = (\sqrt{5} - 1)/2$, and $\delta = \pi/2$. The states are colored according to their fractal dimension (FD). The dashed blue curve indicates the theoretical mobility edge $E = 2\text{sgn}(v)(1 - |v|)/\beta$. (b) Analogous spectral analysis for the mosaic model [Eq. (4)] as a function of parameter λ , computed for $L = 610$ sites with parameters $\alpha = 377/610$ (commensurate approximation [45]), $v = 2$, and $\delta = 0$. Symmetric mobility edges emerge at $E = \pm\lambda$. (c) Quantum metric (blue curve) and energy spectrum with states colored according to their FD for the generalized AAH model at $\beta = 0.8$. (d) Corresponding analysis for the mosaic model at $\lambda = 1.8$.

(b) display the energy spectra and corresponding fractal dimensions for the generalized AAH model and the mosaic model. The colormap encodes the FD of each eigenstate—brighter colors (yellow/red) represent extended or critical states, while darker shades (black/blue) indicate localized ones. The theoretical mobility edges (blue dashed lines) effectively partition the spectra into delocalized and localized regions. Panels (c) and (d), depict the quantum metric $\mathcal{G}(E_F)$ as a function of the Fermi level, which is swept across the energy spectrum by changing the state index below which the states are occupied. At each index, the quantum metric $\mathcal{G}(E_F)$ is calculated via Eq. (12), summing the squared matrix elements of the position operator between occupied and unoccupied states.

These results reveal a clear and universal trend: the quantum metric is suppressed when the Fermi level lies in regions populated by localized states, due to the lack of spatial overlap between them. In contrast, it increases dramatically when the Fermi level enters regions dominated by extended states, where wavefunctions support large fluctuations and spatial correlations. Most importantly, $\mathcal{G}(E_F)$ exhibits sharp transitions at the mobility edges, indicating clear signatures of energy-dependent localization-delocalization transitions.

This behavior confirms the quantum metric as a highly

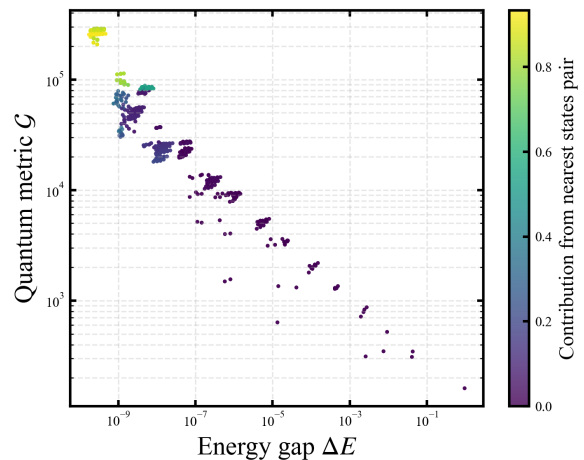


FIG. 4. Relationship between quantum metric and spectral gaps in an off-diagonal FC, with $t_A = 0.1$, $t_B = 1$, and system size $N = 1597$. Each data point represents the quantum metric evaluated with the Fermi energy situated within a spectral gap. The horizontal axis shows the energy gap size ΔE on a logarithmic scale, while the vertical axis displays the corresponding quantum metric $\mathcal{G}(E_F)$ calculated using Eq. (12). The color scale indicates the relative contribution from the pair of states bordering each gap to the total quantum metric. Smaller gaps systematically correspond to dramatically enhanced quantum metric values, with the primary contributions coming from adjacent state pairs bordering the gap.

sensitive probe of mobility edges in quasiperiodic systems. Unlike conventional diagnostics based on FD or inverse participation ratio of each state [52–54], which cannot discriminate the inter-state spatial correlation and long-range coherence, the quantum metric provides a clean, wavefunction-based nonlocal indicator of localization transitions. The consistency of these findings across both the generalized AAH and mosaic models—despite their fundamentally different constructions—points to the universality of this geometric response.

C. Spectral Fractality and Quantum Geometry in the FC

The FC serves as a paradigmatic example of a 1D quasiperiodic system, distinguished by its unique spectral characteristics that fundamentally diverge from those of both periodic crystals and disordered media. Unlike the AAH model, which exhibits a tunable localization transition, the FC remains critical for any nonzero quasiperiodic modulation. Its energy spectrum is singular-continuous—a mathematical structure intermediate between the discrete spectra of finite systems and the continuous bands of periodic systems. This spectrum features a Cantor-like, self-similar hierarchy of energy gaps that span all energy scales.

To explore the interplay between this spectral fractality and quantum geometry, we examined the behavior

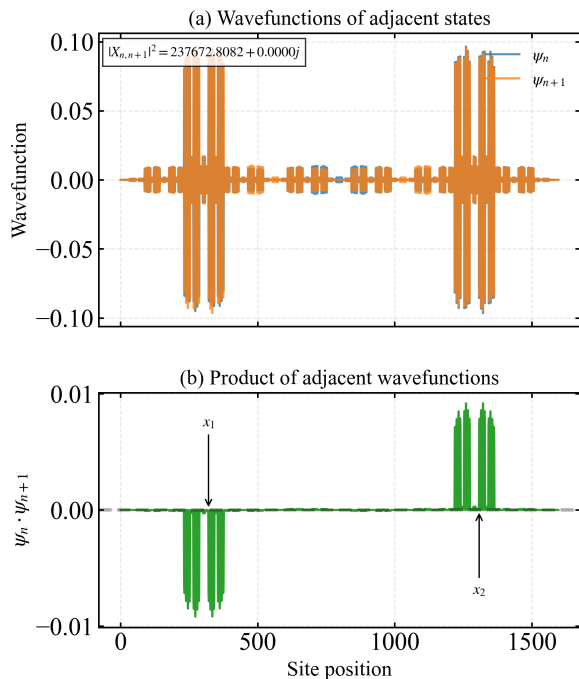


FIG. 5. Microscopic origin of quantum metric enhancement in small spectral gaps of the FC. (a) Almost identical amplitude distribution of two adjacent critical states (ψ_n and ψ_{n+1}) that border a small energy gap where the total quantum metric $\mathcal{G}(E_F)$ reaches its maximum value in Fig. 4. The two states are bonding-antibonding pairs, resulting in a significant quantum metric contribution $g_{\text{pair}} = |X_{n,n+1}|^2$. (b) Product of the two wavefunctions ($\psi_n \cdot \psi_{n+1}$), revealing characteristic spatial centers (x_1, x_2) of the constituent orbitals.

of the integrated quantum metric \mathcal{G} as the Fermi level is tuned within the hierarchical gaps of the FC's fractal energy spectrum. Fig. 4 presents our results for a FC with 1597 sites (corresponding to the 16th generation of the Fibonacci sequence). Each data point represents the quantum metric evaluated with the Fermi energy situated within a spectral gap. The color scale indicates the relative contribution from the pair of adjacent eigenstates—those immediately below and above the gap—to the total quantum metric.

Our analysis reveals a striking inverse correlation between spectral gap size and quantum metric magnitude: narrower energy gaps systematically correspond to larger quantum metric values. This trend suggests an approximate power-law relationship between the gap width and \mathcal{G} , pointing to an emergent scaling behavior inherent in the fractal spectrum. Remarkably, in the limit of minuscule gaps—associated with high-order levels in the spectral hierarchy—the quantum metric can exceed the maximal values achievable in conventional periodic systems.

In configurations where the quantum metric achieves its maximum values, the contribution from the pair of states immediately bordering the Fermi level becomes overwhelmingly dominant, as evidenced by the

color gradient in Fig. 4. These two states are typically bonding-antibonding state pair, approximated as $\psi_{\pm} \sim \frac{1}{\sqrt{2}}(\psi_1 \pm \psi_2)$, with optimized spatial separation and wavefunction overlap to yield exceptionally large quantum metric contributions. This interpretation is further supported by Fig. 5, which shows (a) the spatial profiles of the individual wavefunctions and (b) their product, indicating the characteristic spatial centers (x_1, x_2) of the constituent orbitals. Consequently, the contribution to quantum metric from such a state pair can be theoretically estimated as:

$$g_{\text{pair}} = |\langle \psi_+ | \hat{x} | \psi_- \rangle|^2 = \frac{1}{4}(x_1 - x_2)^2, \quad (14)$$

where the factor of 1/4 arises from the spatial matrix element between the symmetric and antisymmetric combinations of two well-separated, normalized wavefunctions. In the FC, the quasiperiodic modulation naturally generates such widely spaced resonant pairs, amplifying the dipole matrix elements and thereby enhancing the quantum metric.

This pronounced bonding-antibonding character observed near small spectral gaps is deeply connected to the real-space renormalization group (RG) properties of the FC. The system admits a well-defined real-space RG framework, under which its self-similar structure can be systematically simplified while preserving its critical character [39, 40]. In particular, the molecular RG transformation effectively maps strongly coupled site pairs into emergent degrees of freedom—precisely the bonding-antibonding configurations responsible for the enhanced quantum metric near narrow spectral gaps. This intimate connection between spectral fractality, quantum metric enhancement, and RG hierarchy opens promising avenues for a deeper theoretical understanding of enhanced quantum geometry in quasiperiodic systems.

D. Perturbative Renormalization group analysis

To obtain underlying physical insight of the quantum metric enhancement observed in the FC, we employ a perturbative real-space RG approach that exploits the system's inherent self-similar structure [39]. For an off-diagonal FC with strong and weak bonds (denoted by s and w), the lattice can be divided into isolated sites (atoms) and dimers connected by a strong bond (molecules) in the absence of weak bonds. The RG scheme involves two types of decimation procedures that map the original FC Hamiltonian to a lower-order FC with renormalized parameters: (i) An atomic RG transformation that reduces the Fibonacci chain of F_n to F_{n-3} sites; (ii) Two independent molecular RG transformations are applied to the bonding and antibonding states, each producing a renormalized chain of F_{n-2} sites.

Fig. 6 illustrates these two RG procedures. For simplicity, we set the onsite energy $\epsilon_n = 0$ and assume the limit of vanishing weak bonds ($|w/s| \ll 1$). In the atomic

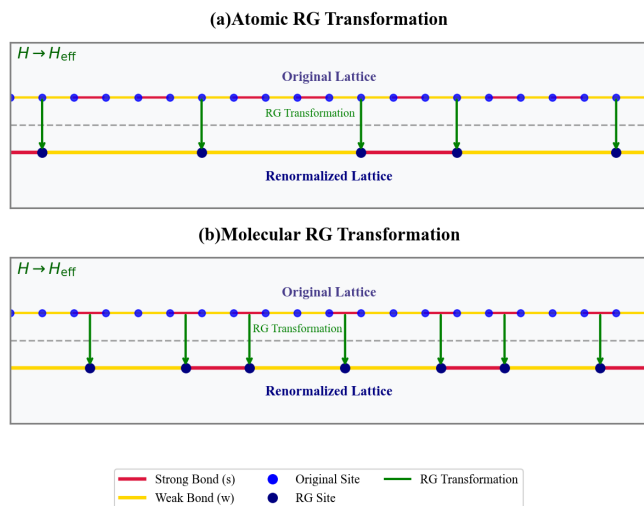


FIG. 6. Renormalization group transformations for the FC. (a) Atomic RG transformation (top panel), where only atomic sites (flanked by weak bonds) are kept, and all other sites are decimated. These sites in the renormalized lattice are connected by effective strong and weak bonds for pairs of atoms separated by one or two molecules in the original lattice. (b) Molecular RG transformation (bottom panel), where molecules (strong bond-connected site pairs) are treated as single effective sites. Effective strong and weak bonds in the renormalized lattices are for these molecules connected by one or two weak bonds in the original lattice.

RG transformation (Fig. 6(a)), atomic sites, which are flanked by two weak bonds, are mapped to new sites in the renormalized lattice, while all other sites are discarded. On the other hand, the molecular RG transformation (Fig. 6(b)) substitutes each strongly-bonded molecule into a new renormalized site, effectively encoding the bonding-antibonding character into the renormalized hopping parameters. After each lattice RG transformation, the new strong and weak bonds, which are determined automatically from their relative lengths in the renormalized lattice, are also arranged in a Fibonacci sequence, giving the renormalized lattice the same structure as the original one. These transformations lead to well-defined recursion relations for the renormalized hopping amplitudes:

$$\mathcal{H}(s, w, F_n) \xrightarrow{\text{atomic}} \mathcal{H}(-w^2/s, w^3/s^2, F_{n-3}) \quad (15)$$

$$\mathcal{H}(s, w, F_n) \xrightarrow{\text{molecular}} \mathcal{H}(\pm w/2, w^2/2s, F_{n-2}) \quad (16)$$

where $\mathcal{H}(s, w, F_n)$ is the Hamiltonian on a FC lattice of F_n sites, s and w represent strong and weak hopping amplitudes, respectively. The sign in the molecular case corresponds to whether the initial molecular state is a bonding ($+w/2$) or antibonding ($-w/2$) state. Because the ratio of two consecutive Fibonacci numbers $\tau_n = F_{n-1}/F_{n-2}$ tends to the golden mean in the large n limit: $\lim_{n \rightarrow \infty} \tau_n = \tau = (1 + \sqrt{5})/2$, the system size N of the renormalized system reduces

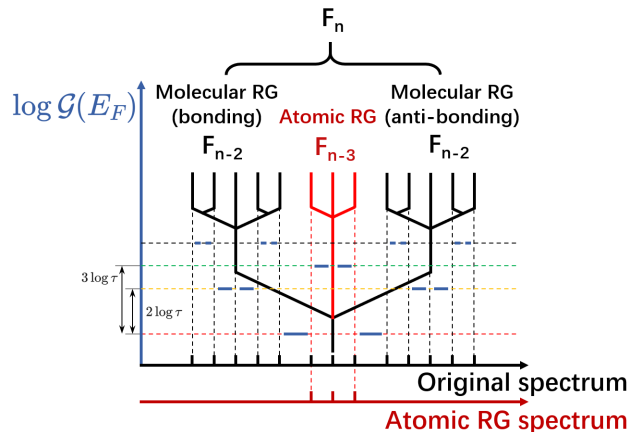


FIG. 7. Schematic illustration of the spectral-splitting pattern for the energy spectra and the hierarchical structure of quantum metric in FC. The ticks on the black (red) horizontal axis denote the eigen-energy for the original lattice (the lattice after an atomic RG transformation). The black cluster of states in the original spectrum can be reproduced by bonding (antibonding) molecular RG, while the red part can be reproduced by atomic RG. The Fibonacci number F_i denotes the number of states (equal to the size of the FC) before and after an RG transformation. The blue vertical axis, along with the short blue segments, denotes the logarithmic quantum metric \mathcal{G} as a function of Fermi energy E_F . The colored dashed horizontal lines denote the hierarchical relation in quantum metric, corresponding to the numerical results shown in Fig. 8.

by a factor of $F_{n-3}/F_n = 1/(\tau_{n-1}\tau_n\tau_{n+1}) \approx 1/\tau^3$ and $F_{n-2}/F_n \approx 1/\tau^2$ for the atomic and molecular RG, respectively [29].

Based on this RG scheme, the Cantor-like spectrum of the original FC as well as the critical nature of the wavefunctions can be fully reconstructed through a sequence of RG transformations applied in the limit of vanishing weak hopping ($|w/s| \ll 1$) [40]. From this RG perspective, smaller gaps in the spectrum emerge after multiple iterations of the RG procedure, representing finer details in the spectral hierarchy. The eigenstates bordering these small gaps remain structurally similar through multiple RG steps before ultimately differentiating into distinct energy levels. This extended similarity through successive RG transformations manifests as stronger spatial correlations between these wavefunctions, directly translating to enhanced quantum metric values when the Fermi level resides within these molecule gaps.

1. Hierarchical Structure of Energy and Quantum Metric Spectrum

To further elucidate the energy spectrum and quantum geometric properties of quasiperiodic systems, we analyze the FC through the lens of real-space RG theory. The FC

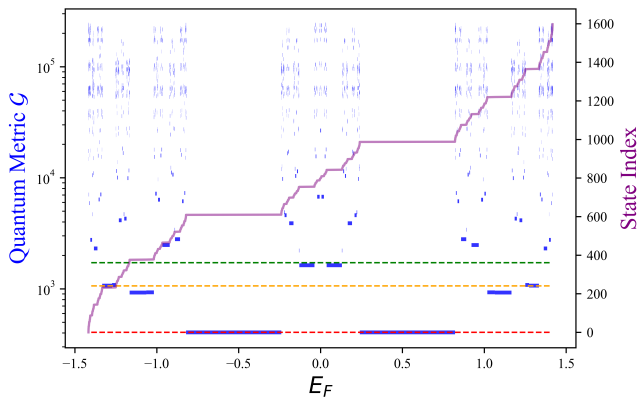


FIG. 8. Quantum metric \mathcal{G} as a function of Fermi energy E_F for a FC with $F_{16} = 1597$ sites. The tight-binding model employs off-diagonal modulation with hopping strengths $t_A = 0.4$ and $t_B = 1$ for weak and strong bonds. The purple curve shows the energy spectrum (state index n vs. Energy E_n). Each horizontal blue segment represents the quantum metric value calculated when the Fermi level lies between adjacent energy eigenvalues. Colored horizontal dashed lines indicate characteristic scaling levels associated with powers of the golden ratio $\tau = (1 + \sqrt{5})/2$: the red line marks the minimum value of \mathcal{G} , while orange and green lines correspond to enhancement factors of τ^2 and τ^3 , respectively—reflecting the scaling behavior under molecular and atomic RG transformations, in accordance with Fig. 7.

exhibits self-similar spectral characteristics that can be systematically understood through RG transformations. As illustrated in Fig. 7, different RG operations generate distinct clusters in the energy spectrum, with gaps separating these clusters. The atomic RG transformation maps the original spectrum’s central region (marked in red) to a rescaled spectrum, while the molecular RG transformation (both bonding and antibonding variants) reproduces the peripheral parts (marked in black). Due to the FC’s self-similarity, we can iteratively apply these RG operations, revealing that each cluster contains sub-clusters separated by higher-order gaps, ultimately giving rise to the fractal structure of the FC energy spectrum.

To investigate how this spectral hierarchy manifests in the quantum metric, we examine the dependence of the quantum metric \mathcal{G} and the Fermi energy, as defined in Eq. (12). As shown in Fig. 8, the results reveal a striking fractal structure in the quantum metric distribution across energy scales. A clear inverse relationship emerges between the size of spectral gaps (reflected in the horizontal extent of flat segments) and the corresponding quantum metric magnitude: large gaps yield small quantum metric values, while small gaps are associated with pronounced quantum metric values. This pattern aligns with our earlier observations in Fig. 4.

More significantly, the fractal structure observed in the quantum metric distribution strongly suggests a fundamental connection to the RG hierarchical organization. Each distinct level in the quantum metric corresponds to

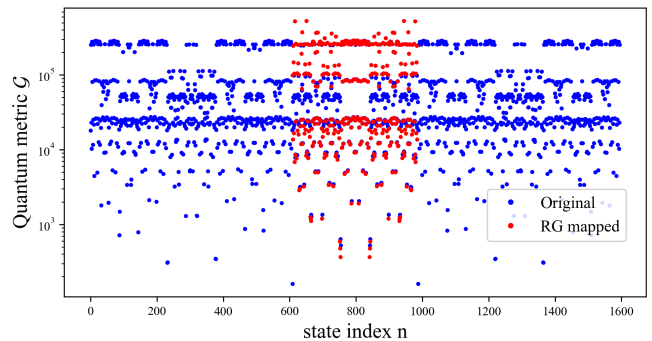


FIG. 9. Validation of the RG mapping of quantum metric in the FC. Comparison between quantum metric calculated from direct numerical diagonalization of the FC with $F_{16} = 1597$ sites (blue circles) and from RG-derived effective Hamiltonian (with $F_{13} = 377$ sites) mapped back to the atomic sites in the original lattice (red circles). The RG-mapped quantum metric, which is shifted to the central region of the energy spectrum ($609 \leq n \leq 978$), agrees well with the corresponding portion of $\mathcal{G}(E_n)$ of the original FC.

a specific tier in the RG tree structure from Fig. 7. In particular, the largest energy gaps, which correspond to separations between atomic and molecular clusters, are associated with the lowest quantum metric values, reflecting the minimal spatial overlap of their corresponding states. By contrast, subgap states within higher-order clusters give rise to increasingly larger quantum metric values, owing to their enhanced spatial coherence and proximity in energy.

Our numerical analysis further demonstrates that the scaling of quantum metric values across successive hierarchical levels follows a power-law relation governed by the golden ratio $\tau = (1 + \sqrt{5})/2$. This scaling behavior is visually emphasized in Fig. 8, where colored horizontal lines denote quantum metric values separated by powers of τ , such as τ^2 , τ^3 , and so on. This correspondence between the quantum metric and RG scaling reveals a deep connection between spatial geometry, spectral fractality, and renormalization flow—underscoring the utility of quantum geometric observables in diagnosing the hidden structure of quasiperiodic systems.

2. Quantum Metric Evolution under RG Transformations

To validate this RG framework in capturing the evolution of quantum metric, we compare quantum metric values computed from RG-based wavefunction reconstruction with those via direct numerical diagonalization. Our RG-based approach proceeds as follows: Taking the atomic RG as an example, we first apply the RG transformation (15) on the F_n lattice, yielding an effective Hamiltonian $\mathcal{H}(-w^2/s, w^3/s^2, F_{n-3})$ in the reduced lattice. We then compute the eigenstates of this renormalized system, map these states back to the atomic sites in

the original F_n lattice, and then evaluate the quantum metric using these reconstructed states. Fig. 9 shows a direct comparison for a FC with $F_{16} = 1597$ sites. Our calculations demonstrate an excellent agreement between \mathcal{G} obtained from RG reconstruction (red points) and that from direct numerical calculations of the original Hamiltonian (blue points) in the central portion of the quantum metric $\mathcal{G}(E_n)$ spectrum. The remaining parts of the spectrum can be reconstructed via molecular RG procedures for bonding and antibonding molecular states. This agreement confirms that the RG method faithfully captures the essential quantum geometric features of the system, despite a significant reduction in degrees of freedom.

It is noted that each RG iteration simultaneously modifies the effective Hamiltonian (through renormalized hopping amplitudes), reduces the system size, and enlarges the averaged bond length a —which rescales the unit of distance. This bond length rescaling and wavefunction reconstruction are crucial for reproducing the quantum metric, since \mathcal{G} has the dimension of length squared and generally scales as $\mathcal{G} \propto a^2$. Importantly, the dominant structure of the wavefunction is preserved under RG flows [39], resulting in \mathcal{G} remaining approximately invariant under successive RG transformations.

To provide a more rigorous understanding of the approximate invariance of \mathcal{G} observed in Fig. 9, we examine the evolution of wavefunctions under RG transformation. Specifically, we introduce a systematic method that reconstructs the wavefunction by tracing the RG sequence in reverse, starting from the final configuration of the RG sequence (see Appendix A). This procedure allows us to theoretically predict the spatial profile wave function as well as the quantum metric for any long FCs. Fig. 10(a) demonstrates the accuracy of this method: the reconstructed wavefunction (blue) agrees remarkably well with the exact eigenstate obtained from direct numerical diagonalization (red) except for weak fluctuation tails, confirming that RG preserves the essential spatial structure of critical wavefunctions.

Using this framework, we computed the quantum metric associated with each energy gap in the RG-reconstructed spectrum. Fig. 10(b) shows that the gap-size dependence of the quantum metric predicted by our RG theory (blue dots) closely matches that from direct calculations (red circles), validating our theoretical approach. This is particularly notable given the substantial computational savings and deeper physical insights provided by the RG perspective.

The most revealing insight appears in Fig. 10(c), where we plot the quantum metric associated with each gap as a function of gap size, color-coded by the number of shared RG operations (i.e., common ancestry in the RG tree) between the two states bordering the gap. A clear pattern emerges: gaps associated with state pairs that share more RG steps (brighter color) systematically exhibit smaller energy separations and larger quantum metric values.

This observation provides a microscopic explanation

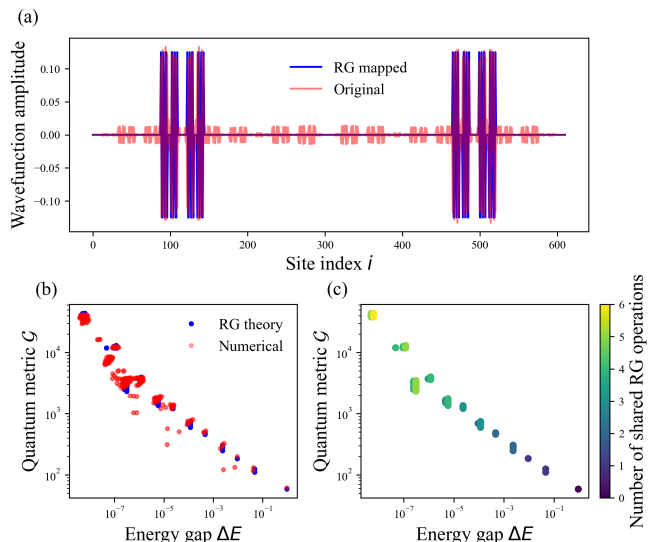


FIG. 10. RG analysis of quantum geometry in the FC. (a) Comparison between the n -th eigenstate wavefunction obtained from direct numerical diagonalization (red) and reconstructed from RG mapping (blue), demonstrating the accuracy of RG methods in capturing critical wavefunction structures. (b) Quantum metric versus energy gap size showing consistent power-law scaling between RG theoretical predictions (blue circles) and direct numerical calculations (red circles). The observed enhancement of the quantum metric for smaller gaps confirms the theoretical relationship derived from RG analysis. (c) Quantum metric as a function of energy gap size, with color coding indicating the number of identical RG operations experienced by both states bordering each gap. States that undergo more shared RG transformations (brighter colors) correspond to smaller gaps and enhanced quantum metric values, providing direct evidence for the spatial correlation mechanism underlying quantum geometric enhancement in quasiperiodic systems.

for the enhancement mechanism: neighboring state pairs that remain nearly degenerate over multiple RG iterations develop strong spatial correlations, resulting in bonding-antibonding structures with large spatial separation and enhanced dipole matrix elements. These features give rise to sharply increased quantum metric values near small spectral gaps, establishing the RG flow history as the key driver of quantum geometric enhancement in quasiperiodic systems.

3. Derivation of the Gap-Metric Relationship via Perturbative RG

The preceding numerical results, obtained through RG analysis, have unveiled a clear physical picture for the mechanism underlying the enhancement and hierarchical organization of the quantum metric in 1D quasicrystals. We now present a theoretical derivation of the relationship between the quantum metric \mathcal{G} and the spectral gap using perturbative RG techniques.

A key ingredient in reconstructing both the wavefunction and the associated quantum metric is the rescaling of bond lengths. In the atomic RG scheme, when an eigenstate of the renormalized Hamiltonian $\mathcal{H}(-w^2/s, w^3/s^2, F_{n-3})$ is mapped back onto the atomic sites of the original FC with F_n sites, the bond length is effectively rescaled by a factor of $\tau_{n+1}\tau_n\tau_{n-1} \approx \tau^3$, where $\tau = (\sqrt{5} + 1)/2$ is the golden ratio. While this geometric rescaling does not alter the hopping amplitudes and therefore leaves the energy spectrum invariant, it leads to an artificial enhancement of the quantum metric by a factor of τ^6 . This behavior is consistent with the fact that the quantum metric is determined by dipole matrix elements between rescaled wavefunctions (see Eq.(14)). A similar argument applies to the molecular RG transformation, which results in a rescaling factor of $\tau_{n+1}\tau_n \approx \tau^2$. These rescaling factors illustrate how the hierarchical decimation of sites and renormalization of couplings naturally give rise to wavefunctions with enhanced nonlocal character [39].

We now turn to the quantum metric at fixed filling for a series of FC lattices. In the Appendix, we prove that the quantum metric satisfies the following recurrence relation:

$$\mathcal{G}(E_F, F_n) = \tau^m \mathcal{G}(E_F, F_{n-m}), \quad (17)$$

where $m = 2$ or 3 for molecular and atomic RG steps, respectively. An intuitive derivation of this scaling is provided in Appendix B, based on the system-size dependence of the minimum quantum metric $\mathcal{G}(F_n) \sim a^2 F_{n-2}/4$, which arises from bonding–antibonding splittings of dimers formed by strong bonds. Physically, this minimum sets the lower bound for the quantum metric, implying that $\mathcal{G} \propto Na^2$ at any fixed filling.

Based on the above analysis, we propose a hierarchical scaling relation for the quantum metric:

$$\begin{aligned} \mathcal{G}(E_F; \mathcal{H}(s, w, F_n), a) &= \mathcal{G}(E_F; \mathcal{H}(Rs, Rw, F_{n-m}), \tau^m a) \\ &= \tau^{2m} \mathcal{G}(E_F; \mathcal{H}(Rs, Rw, F_{n-m}), a) \\ &= \tau^m \mathcal{G}(E_F; \mathcal{H}(Rs, Rw, F_n), a) \\ &= \tau^m \mathcal{G}(R^{-1}(E_F); \mathcal{H}(s, w, F_n), a) \end{aligned} \quad (18)$$

where $\mathcal{G}(E_F; \mathcal{H}(s, w, F_n), a)$ is the quantum metric $\mathcal{G}(E_F)$ obtained via Eq. (12) from the Hamiltonian $\mathcal{H}(s, w, F_n)$ on a FC of F_n sites with bond length a . Rs and Rw denote the renormalized hopping amplitudes under atomic or molecular RG transformations [Eqs. (15) or (16)]. The transformation $R^{-1}(E_F)$ rescales the Fermi energy to preserve the same filling fraction. As shown in Appendix B, this energy rescaling preserves the relative spectral structure, and the possible sign flip in s can be removed via a gauge transformation. Since the quantum metric is a gauge-invariant quantity, it remains unaffected. Thus, Eq. (18) reveals a direct scaling relation between quantum metrics at different Fermi levels in the same FC lattice, highlighting the deep correspondence between the hierarchical structures of the quantum metric and the energy spectrum.

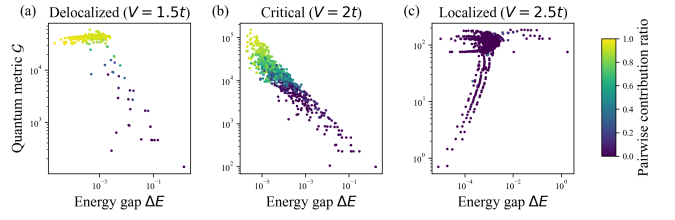


FIG. 11. Quantum metric-gap relationship across different regimes of the AAH model. The quantum metric versus energy gap is plotted for three distinct parameter regimes: (a) delocalized phase ($V = 1.5t$), (b) critical point ($V = 2t$), and (c) localized phase ($V = 2.5t$). Color coding indicates the contribution ratio of the eigenstate pair bordering each gap to the total quantum metric. Only at the critical point (b) does a clear power-law relationship emerge between quantum metric and gap size, mirroring the behavior observed in the FC.

Furthermore, this framework allows us to analytically understand the inverse relationship between quantum metric and spectral gap size observed in Figs. 4 and 10. Under atomic RG transformations in Eq. (15), the renormalized spectral gap transforms as $\Delta E' = \frac{w^2}{s^2} \Delta E$, while the quantum metric transforms as $\mathcal{G}' = \tau^3 \mathcal{G}$. Taking logarithmic derivatives yields:

$$k = \frac{d \log \mathcal{G}}{d \log \Delta E} \Big|_{\text{atomic}} = \frac{3 \log \tau}{2 \log \frac{w}{s}}, \quad (19)$$

Similarly, for molecular RG transformations, we have $\Delta E' = \frac{w}{2s} \Delta E$ and $\mathcal{G}' = \tau^2 \mathcal{G}$, leading to $k = 2 \log \tau / \log(\frac{w}{2s})$. These results predict an approximate power-law scaling $\log \mathcal{G} \sim k \log \Delta E$, quantitatively explaining the nearly linear behavior observed in Fig. 10. This establishes a rigorous theoretical connection between spectral gap size and the quantum metric, rooted in the renormalization structure of the FC.

4. Universality of Quantum Metric Enhancement in Critical Quasiperiodic Systems

To determine whether the observed relationship between gap size and quantum metric is unique to the FC or represents a more universal feature of critical systems, we conducted comparative studies of the AAH model across its three distinct regimes: delocalized, critical, and localized.

As shown in Fig. 11, the delocalized regime ($V = 1.5t$, Fig. 11a) and the localized regime ($V = 2.5t$, Fig. 11c) exhibit relatively low quantum metric values, with no significant correlation between metric magnitude and the energy gap size. In stark contrast, at precisely the critical point ($V = 2t$, Fig. 11b), we observe a pronounced inverse relationship between quantum metric and gap size—an enhancement pattern closely resembling that seen in the FC.

This striking agreement suggests that the enhancement of the quantum metric near small spectral gaps is not merely a feature of quasiperiodicity, but rather a universal signature of criticality. From an RG perspective, this universality arises from the fact that both the FC and the critical AAH model correspond to fixed points characterized by self-similarity and scale invariance. In these systems, RG transformations preserve the structural form of the Hamiltonian while rescaling energy and length scales multiplicatively.

At criticality, this scale invariance ensures that energy gaps and spatial correlations evolve in a coordinated fashion under RG flow: as gaps become smaller through successive RG iterations, the associated wavefunctions become increasingly extended and spatially correlated. This leads to enhanced dipole matrix elements and, consequently, larger quantum metric contributions. Such behavior is absent in the delocalized and localized regimes, where no consistent scaling behavior persists across energy scales.

In both the FC and the AAH model at criticality, the coupling between energy scales and spatial coherence encoded in the RG structure gives rise to a hierarchy of states with long-range correlations and nontrivial geometric response. The emergence of enhanced quantum metric values at small gaps thus serves as a robust diagnostic of criticality, offering deep insight into the structure of critical states.

Our findings highlight a profound and universal connection between criticality, spectral fractality, and quantum geometry. They suggest that quantum metric enhancement arises generically in quasicrystal systems governed by critical states. This universality opens promising trajectories for engineering quantum geometric responses in synthetic systems through targeted manipulation of critical states, offering potential applications in quantum transport, topology, and correlated matter.

E. Optimal quasicrystal configuration for maximal quantum metric

Lastly, we address the question of identifying optimal quasicrystal configurations that maximize the quantum metric. Our analysis starts from a discussion of a topological lower bound on the quantum metric. Recent theoretical advances have revealed that nontrivial band topology imposes a lower bound on the quantum metric in 2D crystalline systems with a nonzero Chern number C . Specifically, the trace of the quantum metric tensor satisfies the inequality $\mathcal{G}_{xx} + \mathcal{G}_{yy} \geq |C|$ [55–57]. This constraint has profound implications for a range of physical observables, including the topological gap, optical conductivity, structure factor, dielectric response, and superfluid weight [23, 24, 26, 55–59]. These results provide a useful guiding principle for the search for 2D topological states with large energy gaps or anomalous Landau level structures [55, 60, 61].

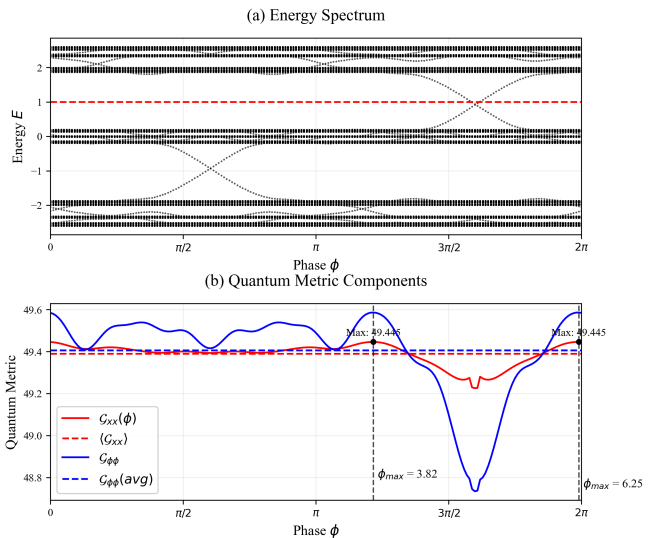


FIG. 12. Energy spectrum and quantum metric versus ϕ for the AAH model. (a) Energy spectrum as a function of phase ϕ . The Fermi energy at $E = 1$ is indicated by the red dashed line. Calculations performed for a 500-site chain with open boundary conditions. (b) Components of the quantum metric tensor: $\mathcal{G}_{\phi\phi}$ (blue solid), \mathcal{G}_{xx} (red dashed). The quantum metric is evaluated at Fermi energy $E = 1$ for a 500-site system with parameters hopping amplitude $V = 2t, \lambda = (\sqrt{5} - 1)/2$

A similar constraint can be formulated for quasicrystals. Notably, the 1D AAH model Eq. (2) can be mapped to the lattice version of the 2D integer quantum Hall effect (IQHE). In this mapping, the electron hops on a 2D rectangular lattice threaded by a perpendicular magnetic field, with a flux ω per plaquette [30, 31]. The 1D AAH model depends on a periodic phase parameter ϕ , which acts as an additional synthetic dimension. The energy gaps of the associated 2D IQHE system are labeled by Chern numbers, as dictated by the gap-labeling theorem [62–65]. Motivated by this mapping, we define the quantum metric in the synthetic 2D parameter space spanned by the real-space coordinate x and the synthetic coordinate ϕ , using Eqs. (7) and (8). This leads to a generalized inequality for 1D quasiperiodic systems:

$$\langle \mathcal{G}_{xx} \rangle + \langle \mathcal{G}_{\phi\phi} \rangle \geq |C|, \quad (20)$$

where $\langle \cdot \rangle$ indicates the average on ϕ over a period of 2π . This connects the quantum geometry across both real and synthetic dimensions in 1D quasicrystalline systems.

This topological bound implies the possibility of optimizing the phason parameter ϕ to maximize the real-space quantum metric component \mathcal{G}_{xx} . Intuitively, for a fixed quasiperiodic modulation strength, a small $\mathcal{G}_{\phi\phi}$ hints a relatively larger \mathcal{G}_{xx} due to the constraint in Eq. (20). As shown in Fig. 12, for a fixed electron filling (i.e., when the Fermi level lies within a given energy gap), we numerically calculate both \mathcal{G}_{xx} and $\mathcal{G}_{\phi\phi}$ as functions of ϕ . Interestingly, both components show similar dependence on ϕ , with significant variation when the

Fermi level crosses topological edge modes in the spectral gap. By scanning over ϕ , we identify an optimal configuration of the 1D quasicrystal that yields the maximal $\mathcal{G}_{xx}(\phi_{max})$. This variation in ϕ corresponds to phason flip-flop transitions between different structural configurations that belong to the same local isomorphism (LI) class [66, 67]. Therefore, the dependence of the quantum metric on ϕ uncovers subtle distinctions among LI-equivalent quasicrystals in terms of their electron localization and quantum geometric response properties.

IV. CONCLUSION

In this work, we have systematically investigated the quantum metric properties of 1D quasiperiodic systems, revealing fundamental insights that bridge quantum geometry with criticality and fractal spectral structures. Our comparative analysis has shown that despite the absence of translational symmetry in both quasiperiodic and disordered systems, the former exhibits significantly pronounced quantum metric than the latter. This stems from the critical nature of wavefunctions in quasiperiodic systems, which maintain long-range correlations and multifractal spatial distributions rather than exhibiting exponential localization characteristics of disordered media.

For the AAH model, we have shown that the quantum metric serves as a sensitive detector of localization transitions, maintaining substantial values in the extended phase while decreasing sharply upon entering the localized phase. More remarkably, in models with mobility edges, the quantum metric distinguishes between delocalized or localized regions of the energy spectrum, providing a potentially measurable signature of energy-dependent localization transitions. This demonstrates the quantum metric's utility as a probe for detecting critical behavior in quasiperiodic systems beyond traditional order parameters.

Our most striking discovery emerges from the FC, where we uncovered anomalously enhanced quantum metric values when the Fermi level resides within minimal gaps of its fractal spectrum. Through perturbative RG analysis, we traced this enhancement to the hierarchical structure of the system and the bonding-antibonding character of critical state pairs bordering these small gaps. We further propose a scaling law on the quantum metric, which quantitatively captures its hierarchical structure. This establishes a profound and previously unrecognized connection between criticality, spectral fractality, and quantum geometry that is absent in either periodic or disordered frameworks.

These findings collectively advance our understanding of quantum geometry in quasiperiodic systems, revealing that quasiperiodicity—positioned at the boundary between order and disorder—fosters unique quantum geometric properties through critical wavefunctions and fractal spectra. The enhanced quantum metric in

these systems suggests potential applications in geometric band engineering, where quasiperiodicity could be leveraged to amplify quantum geometrically-driven responses such as orbital magnetism, nonlinear Hall effects, and superconducting properties mediated by quantum metric.

Future research directions include extending these analyses to higher-dimensional quasicrystals, exploring the interplay between quantum geometry and many-body effects in quasiperiodic systems, and realizing these phenomena experimentally in platforms such as cold atoms, photonic lattices, or engineered metamaterials. As the pivotal role of quantum geometry and topology in condensed matter continues to grow, our work highlights quasiperiodic systems as a promising and versatile platform for realizing novel quantum geometric phenomena beyond the paradigms of crystalline order.

ACKNOWLEDGMENTS

This work is supported by the National Key R&D Program of China (Grant No. 2021YFA1401600), the National Natural Science Foundation of China (Grant No. 12474056), and the 2022 basic discipline top-notch students training program 2.0 research project (Grant No. 20222005). The work was carried out at the National Supercomputer Center in Tianjin, and the calculations were performed on Tianhe new generation supercomputer. The high-performance computing platform of Peking University supported the computational resources.

Note added: During the preparation of the final manuscript, we became aware of the work posted on arXiv [68], which discusses a topic similar to ours.

Appendix A: Detailed Discussion of the Wave Function Reconstruction Procedure

The iterative RG procedure applied to the FC involves, at each step, a choice between three distinct decimation schemes. Each scheme preserves a complementary sector of the energy spectrum. This structure inherently generates a trifurcating tree (see Fig. 7 of the main text), where each RG trajectory corresponds to traversing a specific decimation trajectory from the root vertex. For a finite FC, the RG flow terminates at minimal clusters consisting of either one or two sites—these constitute the endpoints of each trajectory. Crucially, the spectral invariance under RG transformations implies that each distinct trajectory terminating at a minimal cluster identifies one or two unique discrete eigenvalues in the original system's spectrum. Furthermore, the eigenenergy of the Hamiltonian describing the final minimal cluster coincides precisely with the corresponding target eigenvalue in the original spectrum.

A key observation is that each RG step preferentially decimates lattice sites where the corresponding eigenstate has negligible amplitude. This property leads directly to the conclusion that the minimal cluster encapsulates the dominant amplitude components of the original wavefunction. Given that the onsite energy $\epsilon_n = 0$ in our model, the wavefunction for an isolated site is necessarily δ -like. For dimer terminal clusters, the wavefunctions correspond to exact bonding or antibonding states. By recording the history of the decimated FC configuration and the specific RG scheme chosen at each iteration step, we can trace backwards along the RG trajectory. Utilizing the single-site or dimer wavefunctions of the terminal clusters as starting points, the original wavefunction can be reconstructed. Specifically, a single RG step is reversed as follows:

(i). Reversing an atomic RG step: The wavefunction amplitude at the preimage site inherits the value from the image site:

$$\psi_{\text{preimage}} = \psi_{\text{image}} \quad (\text{A1})$$

(ii). Reversing a molecular RG step (bonding or antibonding): The amplitude of the image site unfolds onto the preimage pair according to the projection coefficients defined by the RG scheme:

$$\begin{cases} \psi_{\text{Apreimage}} = \frac{1}{\sqrt{2}}\psi_{\text{image}} \\ \psi_{\text{Bpreimage}} = \pm \frac{1}{\sqrt{2}}\psi_{\text{image}} \end{cases} \quad (\text{A2})$$

where the positive (negative) sign corresponds to reversing a bonding (antibonding) molecular RG transformation.

As an illustrative example, consider starting from an antibonding dimer configuration (Fig. 13), with the initial wavefunction $(\psi_A, \psi_B) = (+\frac{1}{\sqrt{2}}, -\frac{1}{\sqrt{2}})$. Reversing an atomic RG step yields an extended chain configuration with wavefunction amplitudes $(\frac{1}{\sqrt{2}}, 0, 0, -\frac{1}{\sqrt{2}}, 0)$. Subsequently reversing an antibonding molecular RG step decomposes the amplitude $(+\frac{1}{\sqrt{2}})$ associated with the blue site in the previous step into amplitudes $+\frac{1}{2}$ (blue preimage) and $-\frac{1}{2}$ (gray preimage). Similarly, the gray site's amplitude $(-\frac{1}{\sqrt{2}})$ decomposes according to the antibonding projection rule. By iteratively applying this inverse mapping procedure along the recorded RG trajectory, the wavefunction amplitudes on the original lattice are reconstructed.

Appendix B: Scaling of the Quantum Metric in the Strong Dimerization Limit

1. Analytical Solution of \mathcal{G} when E_F Lies in the Largest Gap

We begin by proving the following result which becomes exact in the limit $|w/s| \ll 1$: when the Fermi

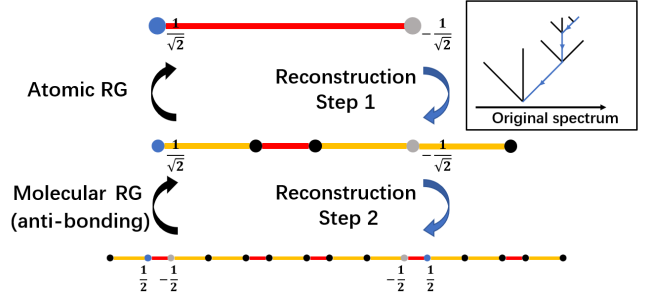


FIG. 13. Illustration of the wave function reconstruction process. Red (yellow) segments denote strong (weak) bonds. Site colors denote wavefunction amplitudes: blue (positive), gray (negative), black (zero); numbers indicate the wavefunction amplitudes on the corresponding sites. Wavefunction reconstruction proceeds sequentially from the top panel (terminal cluster) to the bottom panel (original chain). The inset depicts the reversed RG trajectory in the wavefunction reconstruction procedure (blue arrows).

energy E_{F0} lies in the largest energy gap of a FC with F_n sites and bond length a (see Fig. 14), the quantum metric is given by

$$\mathcal{G}(F_n, E_{F0}) = \mathcal{G}(F_n, -E_{F0}) = \frac{1}{4}F_{n-2}a^2. \quad (\text{B1})$$

Applying this result directly yields $\mathcal{G}(F_{n-m}, E_{F0}) = \frac{1}{4}F_{n-m-2}a^2 = \frac{1}{\tau^m} \frac{1}{4}F_{n-2}a^2 = \frac{1}{\tau^m} \mathcal{G}(F_n, E_{F0})$.

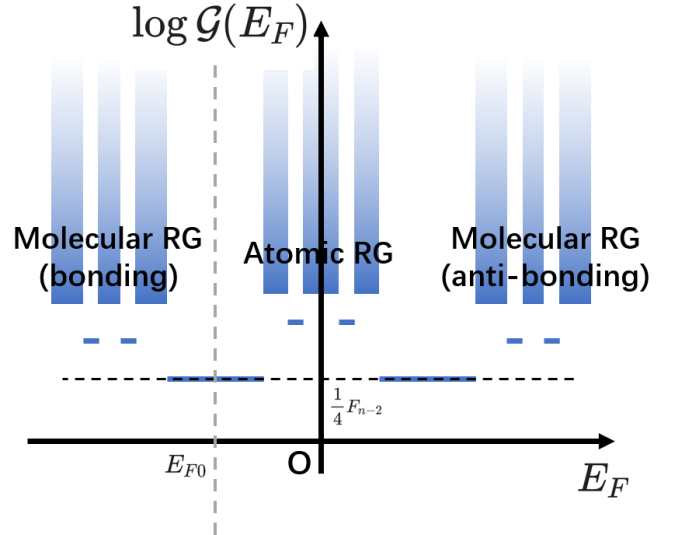


FIG. 14. quantum metric $\mathcal{G}(E_F; H(s, w, F_n), a)$ versus Fermi energy. E_{F0} is marked by the vertical gray dashed line.

The Fermi energy E_{F0} partitions the spectrum into occupied and unoccupied sectors. Crucially, the occupied sector is governed by a bonding molecular RG transformation on the original FC, while the unoccupied states

comprises states associated with atomic and antibonding RG transformations. In the spirit of the bonding molecular RG transformation, we assume that the system is approximately fully dimerized, consisting of bonding pairs connected by a strong bond in the original chain, which we denote as $|n^+\rangle = \frac{1}{\sqrt{2}}(|n\rangle + |n+1\rangle), n \in MC$. Here, for simplicity, we set $a = 1$. MC (AC) denotes sites preserved under molecular (atomic) RG transformations. $|n^+\rangle$ span the occupied subspace. We emphasize that they are *not* eigenstates of the Hamiltonian for $w \neq 0$. Rather, the energy eigenstates are linear superpositions of $\{|n^+\rangle\}$. Similarly, we denote the eigenvectors of the unoccupied states as the linear combination of $|n^0\rangle = |n\rangle, n \in AC$ for the atomic part and $|n^-\rangle = \frac{1}{\sqrt{2}}(|n\rangle - |n+1\rangle), n \in MC$ for the antibonding molecular part, respectively.

Since the set of bonding states forms a complete orthonormal basis for the occupied subspace, the projector onto the occupied subspace can be written as,

$$P = \sum_{i \in occ} |\psi_i\rangle\langle\psi_i| = \sum_{n \in MC}^{F_{n-2}} |n^+\rangle\langle n^+|. \quad (\text{B2})$$

Similarly, the complementary projector admits the decomposition

$$\begin{aligned} \mathbb{I} - P &= \sum_{i \in unocc} |\psi_i\rangle\langle\psi_i| \\ &= \sum_{n \in MC}^{F_{n-2}} |n^-\rangle\langle n^-| + \sum_{n \in AC}^{F_{n-3}} |n^0\rangle\langle n^0|. \end{aligned} \quad (\text{B3})$$

Thus, the quantum metric simplifies to

$$\begin{aligned} \mathcal{G}(F_n) &= \text{Tr}[Px(\mathbb{I} - P)xP] \\ &= \sum_{n \in MC}^{F_{n-2}} \sum_{m \in MC}^{F_{n-2}} |\langle n^+ | x | m^- \rangle|^2 \\ &\quad + \sum_{n \in MC}^{F_{n-2}} \sum_{m \in AC}^{F_{n-3}} |\langle n^+ | x | m^0 \rangle|^2. \end{aligned} \quad (\text{B4})$$

Notice that $\langle n^+ | x | m^0 \rangle = 0$ since AC and MC have nonoverlapping support; therefore, the second term vanishes. The first term in \mathcal{G} is also straightforward to evaluate. By expanding $|n^+\rangle$ and $|m^-\rangle$ on the site basis $\{|n\rangle\}$,

$$\begin{aligned} \langle n^+ | x | m^- \rangle &= \frac{1}{2}(\langle n | + \langle n+1 |)x(|m\rangle - |m+1\rangle) \\ &= \frac{1}{2}\delta_{mn}(m - (m+1)) \\ &= -\frac{1}{2}\delta_{mn}. \end{aligned} \quad (\text{B5})$$

There's no $\delta_{m,n+1}$ or $\delta_{m+1,n}$ term because two strong bonds are not allowed to appear consecutively in the FC.

Thus,

$$\begin{aligned} \mathcal{G}(F_n) &= \sum_{n \in MC}^{F_{n-2}} \sum_{m \in MC}^{F_{n-2}} |\langle n^+ | x | m^- \rangle|^2 \\ &= \frac{1}{4} \sum_{n \in MC}^{F_{n-2}} \sum_{m \in MC}^{F_{n-2}} \delta_{mn} \\ &= \frac{1}{4} F_{n-2}. \end{aligned} \quad (\text{B6})$$

Remarkably, the matrix element contributing to the

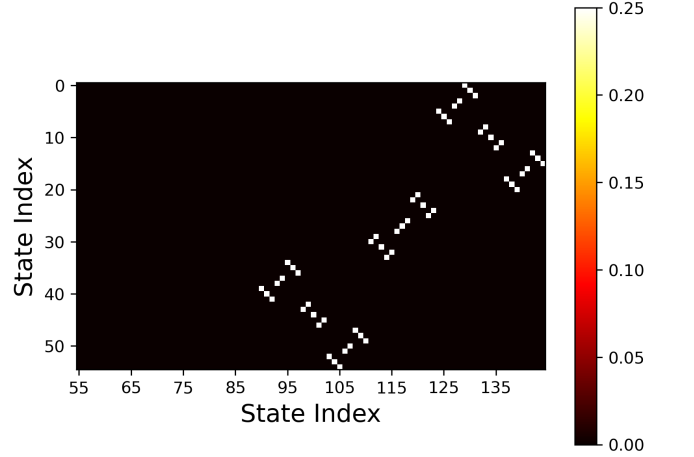


FIG. 15. Color plot of the matrix element $g_{pair} = |\langle \psi_\alpha | x | \psi_\beta \rangle|^2$ contributing to the quantum metric. States numbered 0 to 54 form the occupied states, namely the bonding molecular RG sector, while states numbered 55 to 143 correspond to the unoccupied states.

quantum metric between pairs of occupied and unoccupied eigenstates $\langle \psi_i^+ | x | \psi_j^- \rangle|^2$ exhibits an interesting pattern, as shown in Fig. 15. Namely, for each occupied eigenstate $|\psi_i^+\rangle$, there is a *unique* eigenstate in the unoccupied subspace for which the matrix element is non-vanishing. We note that for each eigenstate in the bonding molecular sector $|\psi_i^+\rangle = \sum_n c_{in} |n^+\rangle$, $|\psi_i^-\rangle = \sum_n c_{in} |n^-\rangle$ is also an eigenstate in the antibonding sector (exact for $w \rightarrow 0$) due to symmetry considerations. The above matrix element is thus evaluated as follows:

$$\begin{aligned} \langle \psi_i^+ | x | \psi_j^- \rangle &= \sum_n \sum_m \frac{1}{2} c_{in}^* c_{jm} \\ &\quad \times (\langle n | + \langle n+1 |)x(|m\rangle - |m+1\rangle) \\ &= \sum_n \sum_m -\frac{1}{2} c_{in}^* c_{jm} \delta_{mn} \\ &= \sum_n -\frac{1}{2} c_{in}^* c_{jn} \\ &= -\frac{1}{2} \delta_{ij}. \end{aligned} \quad (\text{B7})$$

Notice that the orthogonality for eigenstates requires $\sum_n c_{in}^* c_{jn} = \delta_{ij}$. We have thus proved the following result:

$$|\langle \psi_i^+ | x | \psi_j^- \rangle|^2 = \frac{1}{4} \delta_{ij}. \quad (\text{B8})$$

which is in perfect agreement with the numerical result in Fig. 15.

2. Gauge Symmetry of the FC Hamiltonian

The FC Hamiltonian (Eq. (1)) with $\epsilon_n = 0$ exhibits a spectral symmetry: $\mathcal{H}(s, w, F_n)$ and $\mathcal{H}(-s, w, F_n)$ are isospectral. This can be shown by exploiting the following gauge symmetry that relates the two Hamiltonians. Starting from the leftmost dimer, we group adjacent dimers into pairs, as indicated by the blue dashed boxes in Fig. 16. Notice that adjacent strong bonds are intrinsically forbidden in FCs due to quasiperiodic constraints. We then take $c_i \rightarrow -c_i$, $c_i^\dagger \rightarrow -c_i^\dagger$ for all sites in the blue boxes. It's obvious that such a gauge transformation maps $\mathcal{H}(s, w, F_n)$ to $\mathcal{H}(-s, w, F_n)$. We note that

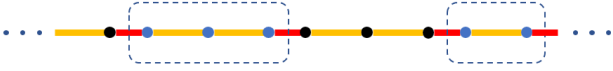


FIG. 16. Illustration of the gauge transformation. Under this gauge transformation, $c_i^{(\dagger)}$ on the blue dots becomes $-c_i^{(\dagger)}$. The red (yellow) bonds denote the strong (weak) hopping amplitude.

the recursion formula in the RG transformations is just a rescaling of the hopping amplitude as well as a possible sign flip of the strong bonds. Because \mathcal{G} is gauge-invariant, we have the following relation for the quantum metric:

$$\begin{aligned} \mathcal{G}(E_F; \mathcal{H}(Rs, R^l w, F_n), a) &= \mathcal{G}(R^{-l}(E_F); \mathcal{H}(\pm s, w, F_n), a) \\ &= \mathcal{G}(R^{-l}(E_F); \mathcal{H}(s, w, F_n), a). \end{aligned} \quad (\text{B9})$$

3. Scaling Relation for \mathcal{G}

Now we are able to give a rigorous proof for Eq.(18). Since each RG step retains one branch of the original trifurcating tree, every gap in the spectrum can be labeled by an RG sequence, such that this gap becomes the largest one at the end of the sequence. Assuming that under this sequential process, we have performed

the RG transformation l times. The final Hamiltonian is $\mathcal{H}(R^l s, R^l w, F_{n-\sum_i^l m_i})$ with a remaining site number $F_{n-\sum_i^l m_i}$, where $m_i = 2$ for molecular RG, and $m_i = 3$ for atomic RG, the bond length changes to $\prod_i^l \tau_i^{m_i} a$. We obtain

$$\begin{aligned} \mathcal{G}(E_F; \mathcal{H}(s, w, F_n), a) &= \mathcal{G}(E_F; \mathcal{H}(R^l s, R^l w, F_{n-\sum_i^l m_i}), \prod_i^l \tau_i^{m_i} a) \\ &= \prod_i^l \tau_i^{2m_i} \mathcal{G}(E_F; \mathcal{H}(R^l s, R^l w, F_{n-\sum_i^l m_i}), a) \\ &= \prod_i^l \tau_i^{m_i} \mathcal{G}(E_F; \mathcal{H}(R^l s, R^l w, F_n), a) \\ &= \prod_i^l \tau_i^{m_i} \mathcal{G}(R^{-l}(E_F); \mathcal{H}(s, w, F_n), a). \end{aligned} \quad (\text{B10})$$

A direct inference of Eq.(B10) implies that $\mathcal{G}(E_F) \propto Na^2$ is valid for any E_F , which is also consistent with Fig. 1(a).

This hierarchical scaling relation for the quantum metric also allows us to understand the inverse relationship between quantum metric and spectral gap size in Fig. 4 and Fig. 10. As a verification of our theory in Eq. (19), we plot the numerical results for the atomic RG transformations, which show a good agreement with the analytical curve, as shown in Fig. 17.

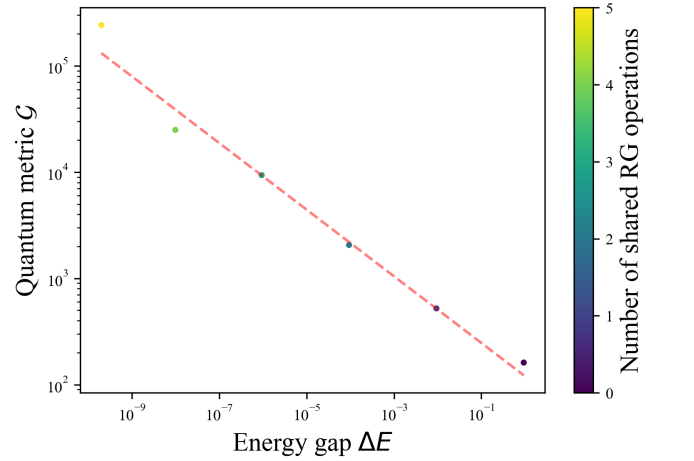


FIG. 17. Quantum metric \mathcal{G} versus energy gap ΔE for atomic gaps in a Fibonacci chain of length $L = 1597$ plotted on logarithmic scales. Points correspond to gaps generated exclusively by atomic renormalization-group operations, colored by the number of shared RG operations. The red dashed line shows a power-law fit $\mathcal{G} \propto (\Delta E)^k$ with exponent $k = \ln(\tau^3) / \ln((t_w/t_s)^2) \approx -0.313$.

-
- [1] J. P. Provost and G. Vallee, Riemannian structure on manifolds of quantum states, *Commun. Math. Phys.* **76**, 289 (1980).
- [2] R. Resta, The insulating state of matter: a geometrical theory, *Eur. Phys. J. B* **79**, 121 (2011).
- [3] N. Nagaosa, J. Sinova, S. Onoda, A. H. MacDonald, and N. P. Ong, Anomalous hall effect, *Rev. Mod. Phys.* **82**, 1539 (2010).
- [4] P. Törmä, Essay: Where can quantum geometry lead us?, *Phys. Rev. Lett.* **131**, 240001 (2023).
- [5] T. Liu, X.-B. Qiang, H.-Z. Lu, and X. C. Xie, Quantum geometry in condensed matter, *Natl. Sci. Rev.* **12**, nwae334 (2024), <https://academic.oup.com/nsr/article-pdf/12/3/nwae334/59204701/nwae334.pdf>.
- [6] J. Yu, B. A. Bernevig, R. Queiroz, E. Rossi, P. Törmä, and B.-J. Yang, Quantum geometry in quantum materials (2025), [arXiv:2501.00098](https://arxiv.org/abs/2501.00098) [cond-mat.mes-hall].
- [7] N. Verma, P. J. W. Moll, T. Holder, and R. Queiroz, Quantum geometry: Revisiting electronic scales in quantum matter (2025), [arXiv:2504.07173](https://arxiv.org/abs/2504.07173) [cond-mat.mtrl-sci].
- [8] R. Cheng, Quantum geometric tensor (fubini-study metric) in simple quantum system: A pedagogical introduction (2013), [arXiv:1012.1337](https://arxiv.org/abs/1012.1337) [quant-ph].
- [9] A. Gao, Y.-F. Liu, J.-X. Qiu, B. Ghosh, T. V. Trevisan, Y. Onishi, C. Hu, T. Qian, H.-J. Tien, S.-W. Chen, *et al.*, Quantum metric nonlinear hall effect in a topological antiferromagnetic heterostructure, *Science* **381**, 181 (2023).
- [10] N. Wang, D. Kaplan, Z. Zhang, T. Holder, N. Cao, A. Wang, X. Zhou, F. Zhou, Z. Jiang, C. Zhang, *et al.*, Quantum-metric-induced nonlinear transport in a topological antiferromagnet, *Nature* **621**, 487 (2023).
- [11] J. Wang, H. Zeng, W. Duan, and H. Huang, Intrinsic nonlinear hall detection of the néel vector for two-dimensional antiferromagnetic spintronics, *Phys. Rev. Lett.* **131**, 056401 (2023).
- [12] D. Kaplan, T. Holder, and B. Yan, Unification of nonlinear anomalous hall effect and nonreciprocal magnetoresistance in metals by the quantum geometry, *Phys. Rev. Lett.* **132**, 026301 (2024).
- [13] K. Das, S. Lahiri, R. B. Atencia, D. Culcer, and A. Agarwal, Intrinsic nonlinear conductivities induced by the quantum metric, *Phys. Rev. B* **108**, L201405 (2023).
- [14] H. Watanabe and Y. Yanase, Chiral photocurrent in parity-violating magnet and enhanced response in topological antiferromagnet, *Phys. Rev. X* **11**, 011001 (2021).
- [15] J. Ahn, G.-Y. Guo, and N. Nagaosa, Low-frequency divergence and quantum geometry of the bulk photovoltaic effect in topological semimetals, *Phys. Rev. X* **10**, 041041 (2020).
- [16] Y. Ulrich, J. Mitscherling, L. Classen, and A. P. Schnyder, Quantum geometric origin of the intrinsic nonlinear hall effect (2025), [arXiv:2506.17386](https://arxiv.org/abs/2506.17386) [cond-mat.mes-hall].
- [17] Y. Jiang, T. Holder, and B. Yan, Revealing quantum geometry in nonlinear quantum materials, *Rep. Prog. Phys.* **10.1088/1361-6633/ade454** (2025).
- [18] R. Roy, Band geometry of fractional topological insulators, *Phys. Rev. B* **90**, 165139 (2014).
- [19] J. Wang, J. Cano, A. J. Millis, Z. Liu, and B. Yang, Exact landau level description of geometry and interaction in a flatband, *Phys. Rev. Lett.* **127**, 246403 (2021).
- [20] B. Estienne, N. Regnault, and V. Crépel, Ideal chern bands as landau levels in curved space, *Phys. Rev. Res.* **5**, L032048 (2023).
- [21] N. Verma, D. Guerci, and R. Queiroz, Geometric stiffness in interlayer exciton condensates, *Phys. Rev. Lett.* **132**, 236001 (2024).
- [22] X. Hu, T. Hyart, D. I. Pikulin, and E. Rossi, Quantum-metric-enabled exciton condensate in double twisted bilayer graphene, *Phys. Rev. B* **105**, L140506 (2022).
- [23] P. Törmä, L. Liang, and S. Peotta, Quantum metric and effective mass of a two-body bound state in a flat band, *Phys. Rev. B* **98**, 220511 (2018).
- [24] F. Xie, Z. Song, B. Lian, and B. A. Bernevig, Topology-bounded superfluid weight in twisted bilayer graphene, *Phys. Rev. Lett.* **124**, 167002 (2020).
- [25] A. Abouelkomsan, K. Yang, and E. J. Bergholtz, Quantum metric induced phases in moiré materials, *Phys. Rev. Res.* **5**, L012015 (2023).
- [26] A. Julku, T. J. Peltonen, L. Liang, T. T. Heikkilä, and P. Törmä, Superfluid weight and berezinskii-kosterlitz-thouless transition temperature of twisted bilayer graphene, *Phys. Rev. B* **101**, 060505 (2020).
- [27] M. Kohmoto, L. P. Kadanoff, and C. Tang, Localization problem in one dimension: Mapping and escape, *Phys. Rev. Lett.* **50**, 1870 (1983).
- [28] S. Ostlund, R. Pandit, D. Rand, H. J. Schellnhuber, and E. D. Siggia, One-dimensional schrödinger equation with an almost periodic potential, *Phys. Rev. Lett.* **50**, 1873 (1983).
- [29] A. Jagannathan, The fibonacci quasicrystal: Case study of hidden dimensions and multifractality, *Rev. Mod. Phys.* **93**, 045001 (2021).
- [30] Y. E. Kraus, Y. Lahini, Z. Ringel, M. Verbin, and O. Zeitler, Topological states and adiabatic pumping in quasicrystals, *Phys. Rev. Lett.* **109**, 106402 (2012).
- [31] Y. E. Kraus and O. Zeitler, Topological equivalence between the fibonacci quasicrystal and the harper model, *Phys. Rev. Lett.* **109**, 116404 (2012).
- [32] D. Tanese, E. Gurevich, F. Baboux, T. Jacqmin, A. Lemaître, E. Galopin, I. Sagnes, A. Amo, J. Bloch, and E. Akkermans, Fractal energy spectrum of a polariton gas in a fibonacci quasiperiodic potential, *Phys. Rev. Lett.* **112**, 146404 (2014).
- [33] S. Aubry and G. André, Analyticity breaking and anderson localization in incommensurate lattices, *Ann. Israel Phys. Soc* **3**, 18 (1980).
- [34] P. G. Harper, Single band motion of conduction electrons in a uniform magnetic field, *Proc. Phys. Soc. London Sect. A* **68**, 874 (1955).
- [35] S. Ganeshan, J. H. Pixley, and S. Das Sarma, Nearest neighbor tight binding models with an exact mobility edge in one dimension, *Phys. Rev. Lett.* **114**, 146601 (2015).
- [36] Y. Wang, X. Xia, L. Zhang, H. Yao, S. Chen, J. You, Q. Zhou, and X.-J. Liu, One-dimensional quasiperiodic mosaic lattice with exact mobility edges, *Phys. Rev. Lett.* **125**, 196604 (2020).
- [37] G. Roati, C. D'Errico, L. Fallani, M. Fattori, C. Fort, M. Zaccanti, G. Modugno, M. Modugno, and M. Inguscio, Anderson localization of a non-interacting bose-einstein condensate, *Nature* **453**, 895–898 (2008).

- [38] D. J. Apigo, W. Cheng, K. F. Dobiszewski, E. Prodan, and C. Prodan, Observation of topological edge modes in a quasiperiodic acoustic waveguide, *Phys. Rev. Lett.* **122**, 095501 (2019).
- [39] Q. Niu and F. Nori, Renormalization-group study of one-dimensional quasiperiodic systems, *Phys. Rev. Lett.* **57**, 2057 (1986).
- [40] Q. Niu and F. Nori, Spectral splitting and wave-function scaling in quasicrystalline and hierarchical structures, *Phys. Rev. B* **42**, 10329 (1990).
- [41] N. Macé, A. Jagannathan, and F. Piéchon, Fractal dimensions of wave functions and local spectral measures on the fibonacci chain, *Phys. Rev. B* **93**, 205153 (2016).
- [42] C. Janot, *Quasicrystals: a primer* (OUP Oxford, 2012).
- [43] T. Janssen, G. Chapuis, and M. De Boissieu, *Aperiodic crystals: from modulated phases to quasicrystals: structure and properties* (Oxford University Press, 2018).
- [44] D. R. Hofstadter, Energy levels and wave functions of bloch electrons in rational and irrational magnetic fields, *Phys. Rev. B* **14**, 2239 (1976).
- [45] X.-C. Zhou, Y. Wang, T.-F. J. Poon, Q. Zhou, and X.-J. Liu, Exact new mobility edges between critical and localized states, *Phys. Rev. Lett.* **131**, 176401 (2023).
- [46] N. Marzari and D. Vanderbilt, Maximally localized generalized wannier functions for composite energy bands, *Phys. Rev. B* **56**, 12847 (1997).
- [47] N. Marzari, A. A. Mostofi, J. R. Yates, I. Souza, and D. Vanderbilt, Maximally localized wannier functions: Theory and applications, *Rev. Mod. Phys.* **84**, 1419 (2012).
- [48] M. S. M. de Sousa, A. L. Cruz, and W. Chen, Mapping quantum geometry and quantum phase transitions to real space by a fidelity marker, *Phys. Rev. B* **107**, 205133 (2023).
- [49] Q. Marsal and A. M. Black-Schaffer, Enhanced quantum metric due to vacancies in graphene, *Phys. Rev. Lett.* **133**, 026002 (2024).
- [50] D. Thouless, Electrons in disordered systems and the theory of localization, *Phys. Rep.* **13**, 93 (1974).
- [51] E. Abrahams, P. W. Anderson, D. C. Licciardello, and T. V. Ramakrishnan, Scaling theory of localization: Absence of quantum diffusion in two dimensions, *Phys. Rev. Lett.* **42**, 673 (1979).
- [52] T. C. Halsey, M. H. Jensen, L. P. Kadanoff, I. Procaccia, and B. I. Shraiman, Fractal measures and their singularities: The characterization of strange sets, *Phys. Rev. A* **33**, 1141 (1986).
- [53] J. Biddle and S. Das Sarma, Predicted mobility edges in one-dimensional incommensurate optical lattices: An exactly solvable model of anderson localization, *Phys. Rev. Lett.* **104**, 070601 (2010).
- [54] Y. Lahini, R. Pugatch, F. Pozzi, M. Sorel, R. Morandotti, N. Davidson, and Y. Silberberg, Observation of a localization transition in quasiperiodic photonic lattices, *Phys. Rev. Lett.* **103**, 013901 (2009).
- [55] Y. Onishi and L. Fu, Fundamental bound on topological gap, *Phys. Rev. X* **14**, 011052 (2024).
- [56] Y. Onishi and L. Fu, Quantum weight: A fundamental property of quantum many-body systems, *Phys. Rev. Res.* **7**, 023158 (2025).
- [57] Y. Onishi and L. Fu, Topological bound on the structure factor, *Phys. Rev. Lett.* **133**, 206602 (2024).
- [58] Y. Onishi and L. Fu, Universal relation between energy gap and dielectric constant, *Phys. Rev. B* **110**, 155107 (2024).
- [59] S. Peotta and P. Törmä, Superfluidity in topologically nontrivial flat bands, *Nat. Commun.* **6**, 8944 (2015).
- [60] X. Long and F. Liu, Interplay of quantum and real-space geometry in the anomalous landau levels of singular flat bands (2025), [arXiv:2505.03024 \[cond-mat.mes-hall\]](https://arxiv.org/abs/2505.03024).
- [61] J.-W. Rhim, K. Kim, and B.-J. Yang, Quantum distance and anomalous landau levels of flat bands, *Nature* **584**, 59 (2020).
- [62] J. Bellissard, Gap labelling theorems for schrödinger operators, in *From number theory to physics* (Springer, 1992) pp. 538–630.
- [63] B. Simon, Almost periodic schrödinger operators: A review, *Adv. Appl. Math.* **3**, 463 (1982).
- [64] N. Macé, A. Jagannathan, and F. Piéchon, Gap structure of 1d cut and project hamiltonians, *J. Phys. Conf. Ser.* **809**, 012023 (2017).
- [65] J. M. Luck, Cantor spectra and scaling of gap widths in deterministic aperiodic systems, *Phys. Rev. B* **39**, 5834 (1989).
- [66] R. Ingalls, Octagonal quasicrystal tilings, *J. Non-Cryst. Solids* **153**, 177 (1993).
- [67] C. Lin, P. J. Steinhardt, and S. Torquato, Hyperuniformity variation with quasicrystal local isomorphism class, *J. Phys. Condens. Matter* **29**, 204003 (2017).
- [68] Q. Marsal, P. Holmval, and A. M. Black-Schaffer, *Quantum metric and localization in a quasicrystal* (2025), [arXiv:2506.15575 \[cond-mat.mes-hall\]](https://arxiv.org/abs/2506.15575).